Carbon 111 (2017) 796–806

Contents lists available at ScienceDirect

Carbon

journal homepage: www.elsevier.com/locate/carbon

Designing graphene based nanofoams with nonlinear auxetic and anisotropic mechanical properties under tension or compression

Andrea Pedrielli [a, b], Simone Taioli [b, c], Giovanni Garberoglio [b, *], Nicola M. Pugno [a, d, e, **]

[a] Laboratory of Bio-inspired & Graphene Nanomechanics, Department of Civil, Environmental and Mechanical Engineering, University of Trento, Via Mesiano 77, 38123 Trento, Italy
[b] European Center for Theoretical Studies in Nuclear Physics and Related Areas (ECT*-FBK) and Trento Institute for Fundamental Physics and Applications (TIFPA-INFN), 38123 Trento, Italy
[c] Faculty of Mathematics and Physics, Charles University, 180 00 Prague 8, Czech Republic
[d] Center for Materials and Microsystems, Fondazione Bruno Kessler, Via Sommarive 18, 38123 Povo, TN, Italy
[e] School of Engineering and Materials Science, Materials Research Institute, Queen Mary University of London, London E1 4NS, UK

ARTICLE INFO

Article history:
Received 16 June 2016
Received in revised form
12 September 2016
Accepted 15 October 2016
Available online 17 October 2016

ABSTRACT

In this study, the analysis of the mechanical response of realistic fullerene-nanotube nanotruss networks with face-centered cubic geometry is performed by using molecular dynamics with reactive potentials. In particular, the mechanical properties of these novel architectures are investigated in both compressive and tensile regimes, a number of truss geometries by straining along different directions. Our atomistic simulations reveal a similar behavior under tensile stress for all the samples. Conversely, under compressive regimes the emergence of a response that depends on the orientation of load is observed together with a peculiar local instability. Due to this instability, some of these nanotruss networks present a negative Poisson ratio in compression, like re-entrant foams. Finally, the performance of these nanotruss networks is analyzed with regards to their use as impact energy absorbers, displaying properties that outperform materials traditionally used in these applications.

1. Introduction

Recent advances in single and multi-layered graphene growth techniques [4,31] have renewed the interest in synthesising carbon-based porous nanomaterials. These materials are promising for a broad range of applications, ranging from energy storage in amorphous structures [1] to tunable hierarchical nanotube scaffolds for regenerative medicine [9], and lightweight foams for oil absorption [38]. Furthermore, pristine graphene shows exceptional mechanical properties, and the ability to retain its initial shape after strain [13]. However, transferring these unique properties to the macroscale still represents a challenge for materials scientists. For reliable structural applications it is essential to build macroscopic 3D architectures preserving the intrinsic properties of the material. This can be achieved through a proper tuning of the porosity and cell geometry which are the main parameters that affect the mechanical properties of porous materials [12].

Carbon nanomaterials with random porosity distributions were initially proposed as a possible means to transfer graphene's unique mechanical properties, such as Young modulus, tensile strength and toughness from the nano- to the macro-scale. Unfortunately, random-pore structures actually exhibit poor scaling of these mechanical properties with decreasing density [18]. Furthermore, they are limited in the number of achievable architectures, due to the uncontrollable porous distribution.

Conversely, in periodic architectures one can expect all nanoscopic components to work in synergy, and thus deliver optimal mechanical properties at larger length scales. In particular, ordered 3D nano-architectures can be designed to realize specific functional properties such as negative [5,17] or flipping Poisson ratio [39] or to obtain a significant increase in gas and energy storage [11,14,16,36].

Nevertheless, the realization of these periodic graphene 3D nanostructures has been achieved for only a few geometries due to the complexity of the synthesis processes. In this regard, one of the architectures of carbon-based materials that can be most easily

* Corresponding author.
** Corresponding author. Laboratory of Bio-inspired & Graphene Nanomechanics, Department of Civil, Environmental and Mechanical Engineering, University of Trento, Via Mesiano 77, 38123 Trento, Italy.
E-mail addresses: garberoglio@ectstar.eu (G. Garberoglio), nicola.pugno@unitn.it (N.M. Pugno).

http://dx.doi.org/10.1016/j.carbon.2016.10.034
0008-6223/

manufactured is based on the face-centered cubic (FCC) geometry (Fig. 1a). Graphene nanostructures with this geometry have been synthesised, for example, by growing graphene on a FCC assembly of silica nanoparticles [42]. Using this approach, a FCC network of hollow graphene spheres in contact each other was obtained. FCC carbon-based structures can also be realized by covering micrometric 3D trusses with graphene using lithography [40].

On the other hand, computer simulations can be used to perform a detailed screening of different architectures and to help our understanding of their specific properties. To achieve this goal, it is of course necessary to model realistic structures and not only those ideally built from regular blocks of fullerenes and nanotubes.

Different 3D carbon-based triply-periodic structures were proposed in past decades [21,35], e. g. schwarzites or Mackay crystals [32,33] obtained by tiling minimal surfaces having negative Gaussian curvature. Several computational models of these structures were developed using a Monte Carlo approach [35] or the Weierstrass representation [32]. Furthermore, recently, the electronic properties of cubic schwarzites [23,29] were investigated from ab-initio simulations.

Here, we present computer simulations of novel graphene nanotruss architectures with a FCC crystal structure (Fig. 2) investigating their mechanical properties with atomistic resolution. Firstly, we compute the stiffness matrix. Subsequently, we perform simulations in tensile and compressive regimes, studying the stress-strain curves as a function of different geometries, with particular consideration to assessing local instabilities and mechanical hysteresis. Furthermore, characteristics of these FCC structures, such as Poisson ratio and scaling relations between the Young modulus and the density, are determined and compared to the performance of standard materials, such as graphite. Finally, since graphene nanotrusses could potentially be suitable for impact energy absorption and be capable of propagating nanoscopic size effects to macroscopic scales, we investigate their energy absorption efficiency.

In designing a three-dimensional graphene-based nanomaterial, we combined ideas from both nanotruss network design and open-cell foams [2]. The former are micrometric structures built by joining struts in a regular fashion (see Fig. 1b), whereas the latter are porous materials in which pores are connected to each other. The periodicity of microtruss networks, particularly in their octet configuration (see Fig. 1b), enables a good scaling of their mechanical properties. In general, microtruss networks can be made by hollow or solid struts, the former displaying – in general – better elastic properties. However, these materials are fragile and tend to break or deform irreversibly under compression, the principal point of failure being the connection between the struts.

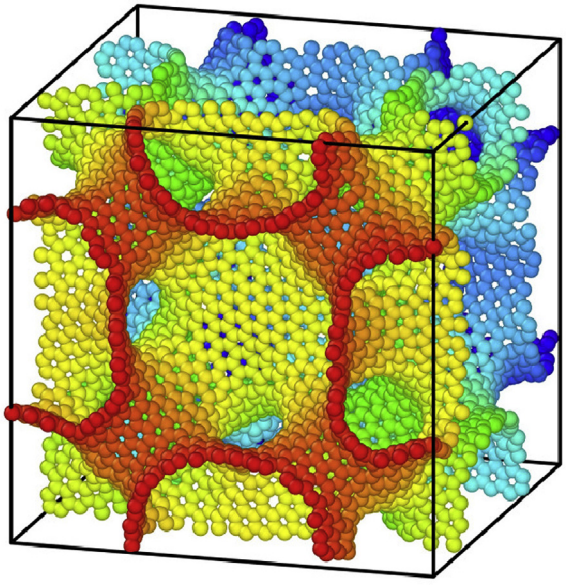

Fig. 2. Unit cell of a graphene nanotruss network with FCC geometry. The faces of the cubic box are perpendicular to the [100], [010], [001] directions. In this figure, the nanotube diameter is 1.1 nm, the sphere diameter is 3.4 nm and the cube edge is 5.5 nm. Colors have been used for visualization purposes only and have no physical meaning. (A colour version of this figure can be viewed online.)

In this paper, we explore the possibility of enhancing the properties of truss networks modifying the way in which the struts are connected. Taking inspiration from the structure of foams, we envisage a nanostructured material in which hollow carbon nanotubes are connected to spheres placed in FCC configurations. Similar materials have already been investigated in the case of body-centered cubic geometry, with emphasis on their mechanical properties under tension [39].

2. Modeling nanotruss geometries

To generate realistic nanotruss networks, we imagine covering a surface composed of FCC spheres (see Fig. 1a) joined by struts in octet-truss geometry [10] (see Fig. 1b) with graphene. The resulting surface is depicted in Fig. 1c.

Although nanotruss geometry is similar to schwarzite's, the latter is characterized by the presence of two separate, while contiguous, subspaces with the same spatial extension. In our case, we do not impose this limitation, allowing these two subspaces to

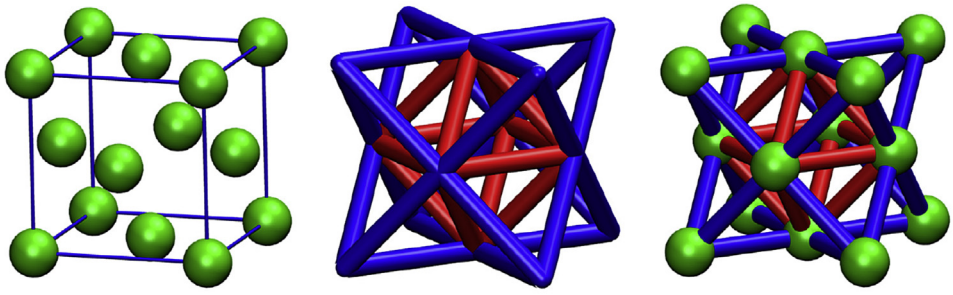

Fig. 1. a) Unit cell with face-centered spheres. b) FCC points connected by sticks to give an octet-truss geometry. (c) Structure obtained by merging a) and b). Subsequently this last geometry was tiled by a graphene net. (A colour version of this figure can be viewed online.)

have different spatial extensions. Indeed, when graphene is grown on stacked nanoparticles, the resulting model is unlikely to represent a structure of minimal surface.

Once the nanotruss structure is defined, we have to perform a surface tessellation to create the actual carbon nanotruss. We achieve this by tiling the surface with regular triangles, then using Voronoi partitioning to dualize it [20,30]. The triangulation is associated with a dense uniform packing, having a fixed lattice spacing, chosen to be almost double the carbon-carbon distance of graphene. This procedure follows closely that reported in Ref. [30], differing in the way the initial triangulation of the surface is achieved. This triangulation was performed using the molecular-dynamics package LAMMPS [24].

A number of points, enough to cover the entire surface, are initially distributed on a regular space-grid (Fig. 3c) and interact with each other via a pairwise Lennard-Jones (LJ) 12-6 potential, with potential parameters ($\sigma = 3.2$ Å, $\varepsilon = 2\times10^{-4}$ eV) and a cutoff of 3.2 Å, such that they behave almost like soft spheres. The choice of the parameters is such that the points in the final dualized configuration are distributed on the surface at a distance close to the carbon-carbon bond length $a_{CC} = 1.42$ Å. The particles were attracted to the surface using a LJ 9-3 potential ($\sigma = 2.0$ Å, $\varepsilon = 1.0$ eV) with a cutoff of 10.0 Å between the points and the surface itself. After relaxation by means of a NVE integration with a viscous damping force (Fig. 3b), the particles distant more than 0.3 Å from the surface were deleted to realize a single layer structure (Fig. 3c). During the whole procedure we imposed periodic boundary conditions, as detailed below.

A number of defects, distributed all over the structure, appear after the LJ triangulation. Here, for defects we intend LJ points having five or seven nearest neighbors. To generate nanotrusses that provide models for sp^2-bonded carbon atoms in graphene, one needs to apply a topological dualization (Voronoi partitioning) to the LJ optimized lattice. We initially computed the adjacency matrix of each particle, where a neighbour was defined as a particle closer than $\sqrt{3} \times a_{CC}$. Distances were evaluated in 3D space and not on the surface. As a final step, we took the Voronoi dual of the points triangulating the surface, using a refining procedure [30] to obtain a configuration of carbon atoms containing only pentagonal, hexagonal and heptagonal rings. These configurations were further annealed by MD with AIREBO-type potentials [27] to obtain the optimized carbon nanotruss networks.

It is worthwhile noting that in evaluating the distances in 3D space the Voronoi dualization automatically smooths possible steps at the intersection between different parts of the surface (e.g. tube-sphere in our case). Heptagonal and pentagonal rings appear in these structures as can be seen in Fig. 2, where we show a unit cell of a model nanotruss obtained using this procedure. In the following, we will refer to pentagonal or heptagonal rings as topological defects.

Nanotruss networks are uniquely defined by fixing the edge length of the cubic box L, the diameter of the nanotubes d and the diameter of the spheres S. Four different structures presenting high connectivity at the nodes (12 in our case) and shown in Fig. 4, have been obtained by modifying these parameters, as reported in Table 1. Using these carbon-based structures, we investigate the dependence of mechanical properties on the sphere and nanotube diameters, and on cell orientation.

In order to study the mechanical properties of these structures as a function of cell orientation, the calculation supercells were obtained by periodically replicating along the [100] direction the unit cell of each structure, by rotating and finally truncating the supercell to obtain configurations with faces perpendicular to the [110] and [111] directions. All considered samples are composed of more than one unit cell to limit the influence of the boundary conditions on the possible reciprocal sliding of the spheres' planes. In this regard, starting from four unit cells, we built four structures for each direction of sampling. The samples obtained using the A, B, C and D unit cells will be numbered from 1 to 4 onwards and are reported in Table 1. The number of atoms in our samples, i.e. in each computational supercell, obtained by periodically repeating the unitary cell along the x, y, and z directions, is dependent on the direction in which they will be loaded. This value is approximately equal to 4×10^4 for the [100] direction, 2×10^4 for the [110] and 3×10^4 for the [111], respectively. Thus, for example, we used a sample composed of $2 \times 2 \times 2$ unit cells to test the nanotrusses in the [100] direction. This is 8 times larger than the unit cell, having approximately 5000 atoms; thus, the number of atoms can be considered of the order of 4×10^4. The dualization procedure was performed on the unit cells to reduce the computational cost, due to its unfavourable scaling with the number of atoms involved. The basic building blocks so obtained were eventually replicated in order to decrease the noise relative to the measured quantities. Furthermore, the supercells were subjected to annealing before calculating mechanical properties to randomize the defects within them.

3. Computational methods

Molecular dynamics simulations were carried out using LAMMPS [24]. The carbon-carbon atomic interaction was modeled through AIREBO potential [27]. Atomic configurations were visualized by using OVITO [28] or VMD [19] package.

The samples were annealed to randomize the presence of defects within the calculation supercell. Samples were first heated at 3500 K and then equilibrated at this temperature for 100 ps. Finally,

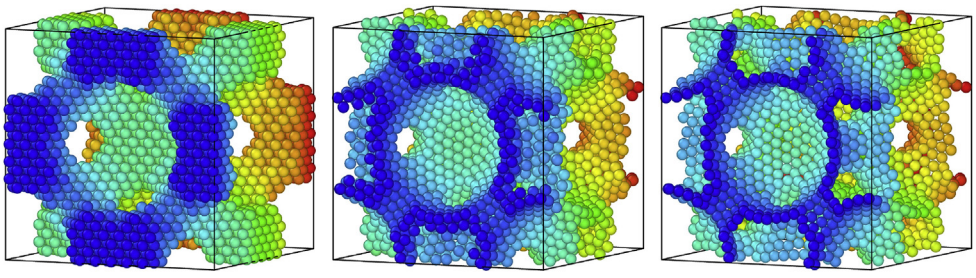

(a) Starting configuration (b) Relaxation of the points (c) Deletion of the points in excess

Fig. 3. The three-step sequence used to triangulate a surface. Panel a) shows the initial condition in which points are arranged in a regular grid. Subsequently, the position of the points is relaxed and they are attracted towards the surface by means of a molecular dynamics run (panel b)). Finally, the points that do not belong to the first layer are deleted to avoid multilayer structures (panel c)). The LJ net is ready for the Voronoi dualization, where it acquires a graphene-like net (see Fig. 2). Colors have been used for visualization purposes only and have no physical meaning. (A colour version of this figure can be viewed online.)

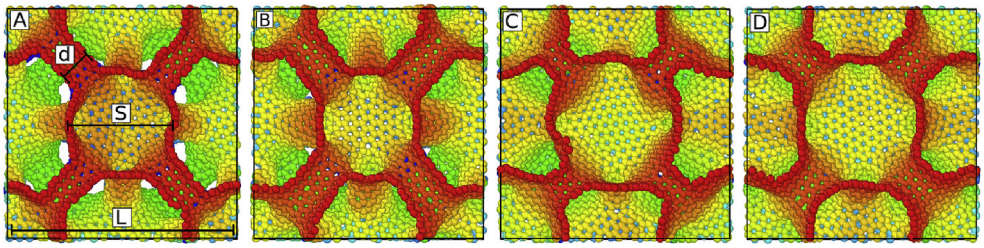

Fig. 4. Side views of the FCC cells. The cube faces are perpendicular to the [100], [010] and [001] directions. The diameter of the nanotubes is 0.8 nm for unit cells A and C, 1.1 nm for B and D. The sphere diameter is 2.7 nm for unit cells A and B and 3.4 nm for unit cells C and D. The box edge is 5.5 nm for all four unit cells. Colors have been used for visualization purposes only and have no physical meaning. (A colour version of this figure can be viewed online.)

Table 1
Parameters used to build the four nanotruss unit cells reported in Fig. 4.

Unit cell	Sphere diameter S (nm)	Nanotube diameter d (nm)	Box side length L (nm)
A	2.7	0.8	5.5
B	2.7	1.1	5.5
C	3.4	0.8	5.5
D	3.4	1.1	5.5

they were cooled down to 700 K in 100 ps using a viscous damping force. The annealing was performed using the standard value for the cutoff parameter for the REBO part of the potential and performed within the microcanonical ensemble (NVE).

We started the mechanical characterization of the samples by computing the stiffness matrix. For linear elastic anisotropic materials the stress and strain tensors are related by a fourth rank tensor, having 21 independent elements, as follows:

$$\sigma_{ij} = C_{ijkl}\varepsilon_{kl} \tag{1}$$

where C is named *stiffness tensor*. In the particular case of cubic symmetry the stiffness tensor has only three terms and the linear system of equations can be written explicitly, as follows:

$$\begin{pmatrix} \sigma_{xx} \\ \sigma_{yy} \\ \sigma_{zz} \\ \sigma_{yz} \\ \sigma_{zx} \\ \sigma_{xy} \end{pmatrix} = \begin{pmatrix} C_{11} & C_{12} & C_{12} & 0 & 0 & 0 \\ C_{12} & C_{11} & C_{12} & 0 & 0 & 0 \\ C_{12} & C_{12} & C_{11} & 0 & 0 & 0 \\ 0 & 0 & 0 & C_{44} & 0 & 0 \\ 0 & 0 & 0 & 0 & C_{44} & 0 \\ 0 & 0 & 0 & 0 & 0 & C_{44} \end{pmatrix} \begin{pmatrix} \varepsilon_{xx} \\ \varepsilon_{yy} \\ \varepsilon_{zz} \\ 2\varepsilon_{yz} \\ 2\varepsilon_{zx} \\ 2\varepsilon_{xy} \end{pmatrix} \tag{2}$$

where the matrix is named *stiffness matrix*.

With regard to the simulations in the compressive and tensile regimes, all samples were equilibrated at zero pressure and at the temperature of 1 K with Nosé–Hoover barostat and thermostat. The adaptive cutoff parameter of the potential has been set to 2.0 Å to better describe the near-fracture regime [26]. The equations of motion were solved with the velocity-Verlet integration method using a time step of 1 fs. Mechanical properties were assessed in the isobaric-isothermal ensemble (NPT), adding a drag term to smooth out the pressure oscillations. The uni-axial tensile strain was applied up to 50% strain that is beyond the fracture strain in each case.

The engineering strain parallel to the direction of deformation is defined as

$$\varepsilon = \frac{L - L_0}{L} = \frac{\Delta L}{L} \tag{3}$$

where L_0 and L are the starting and current length of the sample in the direction of loading. To determine the stress, the pressure stress tensor components in response to the external deformation are computed as [34].

$$P_{ij} = \frac{\sum_k^N m_k v_{k_i} v_{k_j}}{V} + \frac{\sum_k^N r_{k_i} f_{k_j}}{V} \tag{4}$$

where i and j label the coordinates x, y, z; k runs over the atoms; m_k and v_k are the mass and velocity of k-th atom; r_{k_i} is the position of k-th atom; f_{k_j} is the j-th component of the total force on the k-th atom due to the other atoms; and V is the volume of the simulation box. The pressure in Eq. (4) includes both kinetic energy (temperature) and a virial term. Notice that the force appearing in Eq. (4) is the sum of the pairwise, angle, dihedral, improper and long-range contributions. The computed stress is the *true stress* because the pressure is measured with respect to the instantaneous section area of the samples. The uni-axial compressive strain was applied up to 25% and 50% total strain. The applied strain rate is chosen to be 0.001 ps^{-1}, so as to converge the Young modulus and tensile strength, as shown in Fig. 5. Stress and strain were saved every 1000 time steps.

The stress-strain curve was computed at 1 K, since molecular dynamics is usually computationally faster than using a minimization procedure. The same approach has previously been adopted by other groups dealing with similar problems (e.g. Ref. [39]). This introduces a small kinetic contribution, which is approximately 2% of the total stress, almost uniformly distributed along the stress-strain curve. Local maxima of the kinetic contribution up to 4% of the total stress can be found at the points where the structures collapse, due to the small temperature increase. The influence of the kinetic term is clearly small enough to have negligible effect on our simulations.

The features that we calculate to characterize the mechanical properties of the nanotrusses are, in addition to the stiffness tensor, the Young modulus, fracture stress and fracture strain. The toughness is also evaluated as the area under the stress-strain curve up to the fracture stress. Indeed, the samples have no plastic deformation but several sequential fractures. Stress-strain curves of carbon nanotrusses do not present a completely linear behavior (Fig. 5). Thus, the definition of only one slope does not guarantee an accurate fit of this curve and we are forced to introduce two different values of the Young modulus to characterize the mechanical behavior. In particular, the first value of the Young modulus (E_1) is obtained as the tangent at zero strain, while the second one (E_2) from a linear fit between 5% and 8% strain.

We also performed the calculation of the Poisson ratio ν, defined as the negative ratio between the transverse deformation ε_T and the longitudinal one ε_L:

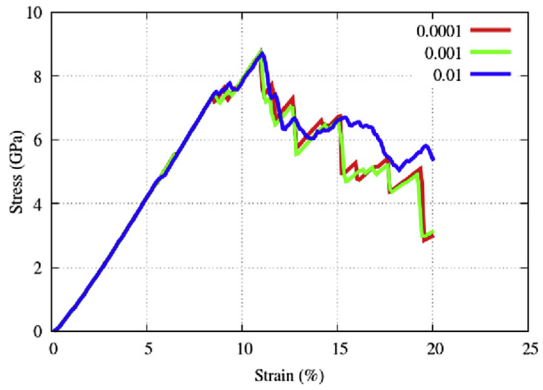

Fig. 5. Stress-strain curve dependence on strain rate in ps^{-1} for the [100] unit cell 4. (A colour version of this figure can be viewed online.)

$$\nu = -\frac{\varepsilon_T}{\varepsilon_L} \tag{5}$$

Here we extend the concept of Poisson ratio to deformations beyond the linear regime, and use it to quantify the lateral deformation of the material. A similar extension is done for the Young modulus.

4. Results and discussion

4.1. Stiffness matrix

The elastic properties of the nanotrusses were first assessed by computing the stiffness matrix. The kinetic energy is not present in the calculation of the stiffness matrix, as this computation was performed using molecular mechanics simulations without a temperature term. The outcome of this computation will also be useful to check if the choice of the structures represents a realistic model of these materials. Indeed, the stiffness matrix of realistic systems can be used to measure the degree of anisotropy by comparison with a perfect FCC cubic cell. The computed stiffness matrix for the sample 3, with faces perpendicular to the [100], [010] and [001] directions, is:

$$\begin{pmatrix} 63.0 & 12.3 & 13.2 & -0.43 & 0.19 & -0.92 \\ & 58.9 & 12.4 & -0.28 & 0.28 & -1.14 \\ & & 58.5 & 0.59 & 0.97 & 0.32 \\ & & & 14.0 & 0.11 & 0.71 \\ & Sym & & & 14.6 & -0.40 \\ & & & & & 13.9 \end{pmatrix}$$

where the values are reported in GPa.

The match with the cubic material stiffness matrix in Eq. (2) is not perfect, as small non-zero terms appear in the upper right part of the matrix. Additionally, terms that must be in principle equal show not negligible discrepancies. The reason of this anisotropy is principally due to the choice of the cell dimension used for the Voronoi tessellation of the surface. Applying the dualization to a single unit cell, the graphene net has to be periodic over a distance of the box edge L and the space available to accommodate the defects is quite small.

4.2. Tension

The mechanical properties of nanotruss networks, such as Young modulus, fracture strain and tensile stress, were further investigated via the assessment of their stress-strain curves. In Fig. 6, we report the stress-strain curve for the four samples along the direction [100] and in Fig. 7 three snapshots of sample 4 under tension.

The stress-strain curves show a typical elastic behavior for small deformations up to the tensile strength (snapshots a and b in Fig. 7), followed by a descending part that corresponds to the fracture of the samples (snapshot c in Fig. 7). The absence of a plastic plateau and instead the presence of a sharp maximum in the stress means that nanotruss networks display the brittle nature of the parent material, i.e. graphene.

In this study we do not attempt to extract information from the part of the stress-strain curves beyond the fracture strain. Indeed, unlike the Young modulus or specific toughness, the crack propagation can be strongly influenced by the size of the simulation box and periodic boundary conditions.

All the curves present a fracture strain of about 10% so that the tensile strength is roughly proportional to the Young modulus. The network with the largest nanotube and sphere diameters (4) has a larger Young modulus and tensile strength than sample 1, which present the smallest values (Fig. 6). The other two cases give comparable results. A similar response is found for the [110], and [111] directions.

The values of Young modulus, tensile strength and fracture strain are reported in Table 2. We also report the values for graphene as calculated using the AIREBO potential (cutoff set to 2.0 Å) in Ref. [43]. We see an increase of the Young modulus and tensile strength for evidently more optimized structures, passing from sample 1 to sample 4. The shape and dimension of the nodes play an important role in the deformation of hollow truss networks, as recently shown for microtruss networks [25,37].

The stiffening behavior (i.e. parabolic shape of the stress-strain curve in the elastic regime) is due to the realignment and bending of the struts at lower strain, and the stretching-dominated deformation of the realigned struts at higher strain, as noted in Ref. [39] for similar structures. In this regard we can study the stiffening using the ratio between the Young modulus E_2 and E_1, which has the highest value for sample 1 (1.61). Samples 2 a 3 give comparable results (1.37, 1.33). For the last sample (4) we find the lowest value (1.19). We underline the similarity between the behavior of samples 2 and 3 in tension in contrast to what will occur in the compressive

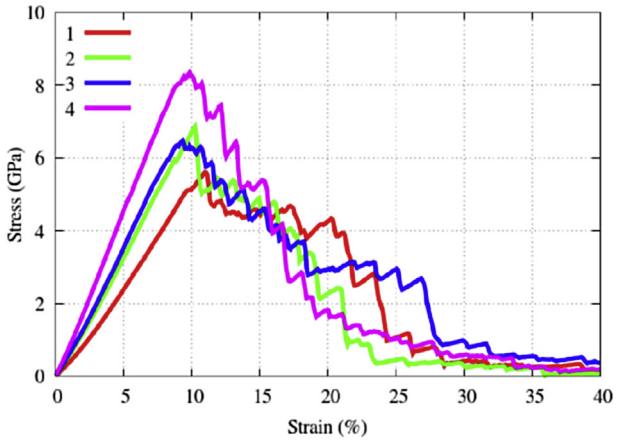

Fig. 6. Stress-strain curves of the four nanotruss networks under uni-axial tension along the [100] direction. The four curves present a Young modulus roughly proportional to the tensile strength and a fracture strain of about 10%. Because the crack propagation can be strongly influenced by the size of the simulation box and by the periodic boundary conditions, the part of the curves beyond the maximum of stress should be taken into account for a physical interpretation of size effects. (A colour version of this figure can be viewed online.)

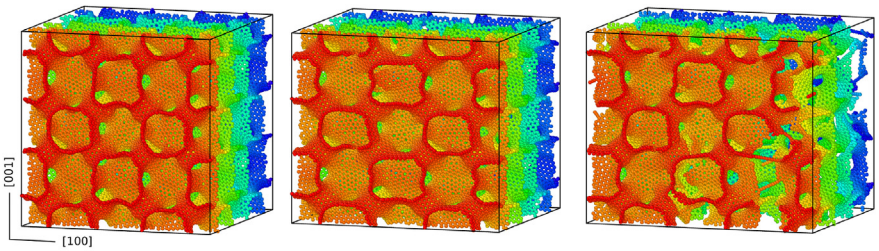

(a) 0% strain (b) 10% strain (c) 20% strain

Fig. 7. Images of sample 4 under traction in the [100] direction. The sample is built by replicating the unit cell D in the space building up a 2 × 2 × 2 unit cell (a). The deformation is applied in the [100] direction. At 10% strain the sample is near to the maximum stress and failure strain where cracks start to grow (b). In image (c), at 20% strain, cracks are larger and there is not only one fracture but cracks formed in many positions. Colors have been used for visualization purposes only and have no physical meaning. (A colour version of this figure can be viewed online.)

Table 2
Young modulus, ultimate strength, and fracture strain of the systems studied under tension along the [100] direction. These values are compared with the average of those reported for armchair and zigzag graphene using AIREBO potential [43].

Sample	Young modulus E_1 (GPa)	Young modulus E_2 (GPa)	Tensile strength (GPa)	Fracture strain (%)
1	36	58	5.6	11.1
2	54	74	6.8	10.2
3	58	77	6.5	9.3
4	79	92	8.3	9.8
Graphene	10^3	10^3	98.5	16.5

case. In fact, they have different geometries but almost the same mass density.

In Table 3 we report the specific modulus and specific strength, which define the values per mass density. Furthermore, in the same table is reported the specific toughness, calculated as the total area under the stress-strain curves up to fracture strain, per mass density. By comparing Tables 2 and 3, we note that even though the Young modulus and tensile strength for the nanotrusses are respectively two and one order of magnitude smaller than those reported for graphene, we obtain a different scenario when considering the specific strength and the specific modulus. The density of these nanotruss networks is about one third of that of graphite, thus enhancing the specific mechanical properties of these materials with respect to graphite.

Considering Fig. 7, we note that cracks propagate from defective sites such as a pair of heptagons. The presence of defective sites is responsible for the small value of the fracture strain, compared to graphene. Furthermore, for defected carbon nanotrusses, like those studied in this work, crack propagation is diffuse, in contrast with ideal materials. Indeed, for ideal nanotube-fullerene networks cracks are preferably localized at the nanotube-fullerene junctions [39].

In the next section we will focus on the compressive regime in which a geometry-dependent behavior emerges more strongly than in the tensile one.

4.3. Compression

In this section we present the results obtained for the samples under compressive load. Contrary to the tension case, the compressive response is strongly related to the nanotruss geometry as well as the direction of compression. In Fig. 8 we report the stress-strain curve in compression along the [111] direction, which presents the most interesting features. The deformation reaches 50% strain for the largest compression, for which the main features of the compressive response are shown.

Indeed, observing Fig. 8, the stress-strain curves are basically characterized by three regimes, typically found in foams and energy absorbing materials. At small strains an elastic region is observed, and the material is characterized by a full recovery to the original shape when the load is removed. Subsequently we observe a plateau, representative of the sample collapse at a nearly constant stress, by buckling or fracture of the building blocks (nanotubes and graphene spheres). Finally, one finds a steep ramp in the stress-strain curve, representing full collapse or a densification regime of the structures.

The four samples reported in Fig. 8 behave similarly in the elastic regime. However, samples 2 and 3 present an inverted response with respect to traction, and the stress for sample 2 in compression is higher than that for sample 3. In the plateau, a geometry-related response occurs. Sample 1 shows a nearly flat plateau that does not approach the densification regime up to 50%

Table 3
Density, specific modulus and specific strength of the four samples studied under tensile strain along the [100] direction. Specific toughness is calculated as the area under the stress-strain curve up to fracture strain per mass density.

Sample	Density kg m^{-3}	Specific modulus 1 (MNm kg^{-1})	Specific modulus 2 (MNm kg^{-1})	Specific strength (MNm kg^{-1})	Specific toughness (MJ kg^{-1})
1	634	57	91	8.8	0.5
2	707	76	105	9.6	0.5
3	705	82	109	9.2	0.4
4	692	114	133	12.0	0.6
Graphite	2250	444.4	444.4	43.8	–

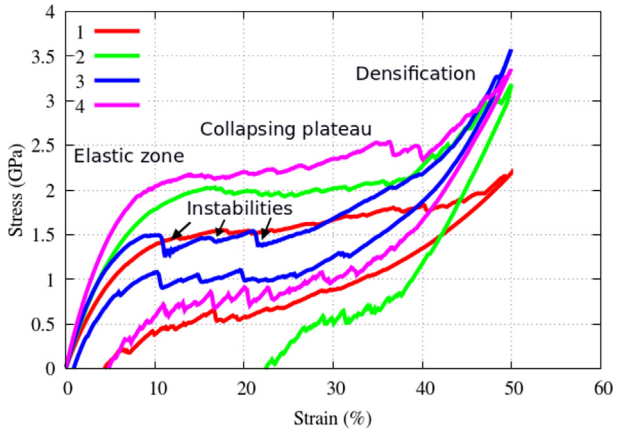

Fig. 8. Stress-strain curves of the four nanotruss networks under uni-axial compression along the [111] direction up to 50% strain. At higher stress one finds the compressive part of the curve, while the unloading part is at lower stress. (A colour version of this figure can be viewed online.)

strain. Samples 2 and 4 present a collapsing plateau before approaching the densification regime at high strain. For samples 1, 2 and 4 one can see from the unloading part of the stress-strain curve that the deformation is partially plastic, without full recovery of the original shape at zero stress. This is a clear signature of mechanical hysteresis in these systems.

Sample 3 presents a response that is very different from the other samples, showing a number of peaks in the plateau of the stress-strain curve (Fig. 8). Each peak is related to the collapse of a plane, as shown in Fig. 9. This type of response, peculiar to sample 3, was found only along the [111] direction. It is worthwhile noting that this response depends on the ratio between the nanotube and the sphere diameters. The collapse of the planes is essentially elastic, indeed the sample presents only a small residual deformation at zero stress.

Finally, we note that the partial insertion inside the sphere of the nanotubes that carry the compressive load is caused by a global instability of the sphere's planes: all the nanotubes that are loaded in compression are influenced in the same manner.

The centers of the graphene spheres divide the space into two volumes of different shape: an octahedron (rendered in red in Fig. 1b) and a tetrahedron (rendered in blue in Fig. 1b). These two volumes are reported in panel a) in Fig. 9. The tetrahedrons are loaded from one vertex towards the center of their base, forcing the nanotubes to rotate during the compression. The load acts in the direction of stabilizing the structure as, remarkably, the samples do not present reciprocal sliding of spheres' planes. This means that further simulations in this load direction could be performed on a single unit cell without loss of generality. Indeed, for samples in which a transverse sliding of the planes is present, the boundary conditions as well as the parity of the number of planes in the simulation cell play a critical role. In the simplest case of a unit cell with only one plane, for example, the sliding is completely prevented.

In Fig. 10 the compressive stress-strain curves up to 25% strain are reported. The unloading part of the curve for sample 3 presents some stress peaks due to the repositioning of nanotubes into their original positions. The number of oscillations is related to the number of planes in the sample; therefore, in the limiting case of a bulk material, we expect that the number of oscillations will increase, resulting in a flat plateau.

Full recovery after compressive deformation similar to that found for sample 3 has been reported, for example, in carbon

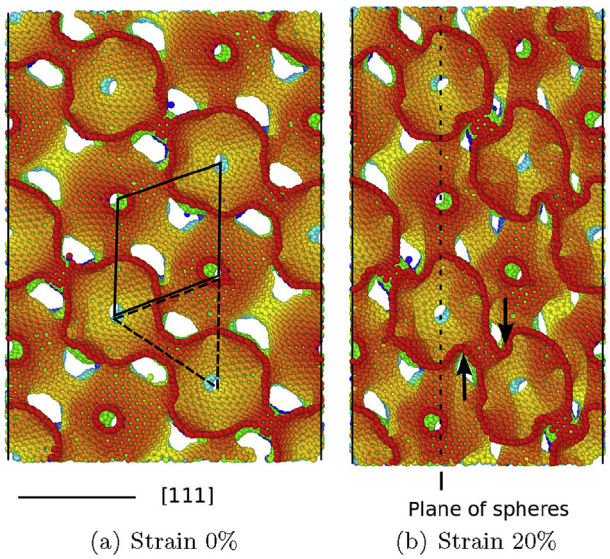

Fig. 9. Nanotruss network number 3 under uni-axial compression along the [111] direction. The first image is the undeformed sample; the second is a snapshot at 20% strain. The centers of the graphene spheres divide the space into two volumes of different shape: an octahedron (rendered in red in Fig. 1b) and a tetrahedron (rendered in blue in Fig. 1b). These two volumes are reported in image a). It is clear from image b) that the tetrahedrons are loaded from one vertex towards the center of their base so that the nanotubes are forced to rotate during the compression. Notice the collapse of the planes of spheres in the second image. In particular, for each plane collapsed there is a peak in the stress-strain curve as reported in Fig. 8. Colors have been used for visualization purposes only and have no physical meaning. (A colour version of this figure can be viewed online.)

nanotube bundles [7] and in ultralight boron nitride foams [41]; in these systems, the deformation in absence of plastic strain is allowed by rotation of the internal components.

In Table 4 we report the Young modulus, plateau stress and residual deformation of the four samples, under uni-axial compression in the [111] direction.

In the next section we will focus on a quantitative evaluation of the Poisson ratio for the samples 3 and 4 in the [110] direction, for which an auxetic response emerges.

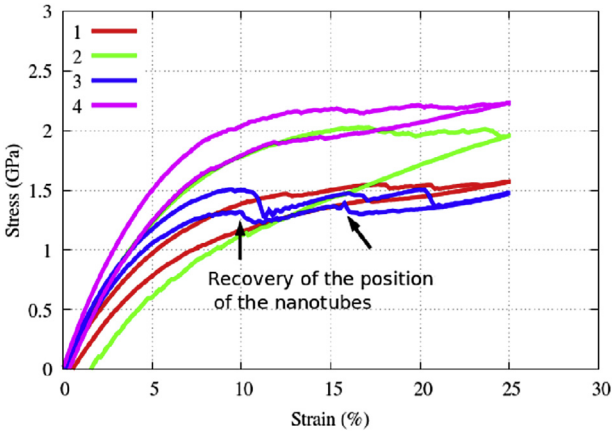

Fig. 10. Stress-strain curves of the four nanotruss networks under uni-axial compression along the [111] direction up to 25% strain. The compressive part of the curve is that at higher stress, the unloading part at lower stress. Sample 3 presents a stress-strain curve qualitatively different from the other samples. It presents three peaks in the loading part of the curve and two peaks in the unloading part. These peaks are due to the global instability of the planes of spheres, as shown in Fig. 9. (A colour version of this figure can be viewed online.)

4.4. Negative Poisson ratio

The quantity characterizing the materials' response in the direction orthogonal to compression is the Poisson ratio ν, defined as the ratio between the negative transverse and longitudinal strain. Commonly, materials have a positive Poisson ratio, meaning that they expand in the direction orthogonal to the external compressive load (e.g. steel, $\nu = 0.3$). Under compression in the [110] direction we found a negative Poisson ratio for samples 3 and 4.

This negative Poisson ratio is strictly connected to an interesting feature, not present in the compression along the other directions, that can be found in the [110] direction. This characteristic, sketched in Fig. 11 for sample 3, is the longitudinal insertion of the nanotubes inside the spheres. Nevertheless, the stress-strain curve in the [110] direction does not show particular features, like the peaks founded for sample 3 in [111] direction, as the load is carried by the other nanotubes. This local instability, related to a single nanotube and not to a whole plane of spheres, has also been found in sample 4 along the [110] direction.

Our simulations also show that the nanotube insertion presents three stable configurations. In two of these configurations, only the bottom part of the nanotube enters one of the adjacent spheres, while in the third one both top and bottom sides of the nanotubes are inserted. We note that this behavior introduces a new degree of freedom under compression for each nanotube aligned with the [110] direction.

In Fig. 12 we report two snapshots of a single sphere of sample 3 under compression. The insertion increases the local curvature of the surface, and, as for the [111] direction, this could be useful to enhance the adsorption or desorption of gases. Due to the symmetry of the structure, the nanotubes in the horizontal plane perpendicular to the [110] direction are free to move under a second load applied in the direction [−110]. For longer nanotubes, the inserted extremities could interact with each other giving collective patterns in the horizontal plane, in particular under bi-axial compression (in directions equivalent to the [110] and [−110] directions).

We report in Fig. 13 the Poisson ratio for samples 3 and 4 under uni-axial compression in the [110] direction. The Poisson ratio is monotonically decreasing in both the samples. Indeed, these two structures are characterized by positive values of ν for small strain in the [−110] and [001] directions. At higher strain, the Poisson ratio of sample 3 along the [−110] and [001] directions presents a minimum at around 35% strain. A similar trend is found for sample 4 with the presence of a plateau starting from 20% strain. Furthermore, we note that Poisson ratios along the z direction become negative. A negative Poisson ratio means that, if a compressive load is applied in the [110] direction, the material tends to increase its density under the applied load. This feature of carbon foams could be useful for delivering effective high-impact energy absorption. Finally, we note that in this case the compressive load tends to stabilize the structure only for small strain, conversely for high strain, a sliding of the spheres' plane is found.

Table 4
Young modulus, plateau stress, and residual deformation of the four samples under uni-axial compression in the [111] direction.

Sample	Young modulus (GPa)	Plateau stress between 10 and 40% strain (GPa)	Residual deformation 25% (%)	Residual deformation 50% (%)
1	27	1.6	0.6	4
2	33	2.0	1.5	22
3	36	1.6	0.2	1
4	42	2.3	0.4	5

4.5. Density scaling relation

The Young modulus E of microstructures obeys a semi-empirical power-scaling law with relative density as follows [2]:

$$\frac{E}{\tilde{E}} = \alpha\left(\frac{\rho}{\tilde{\rho}}\right)^{\beta} \tag{6}$$

where $\tilde{E}$ and $\tilde{\rho}$ are the Young modulus and the density of the bulk material respectively, α is a proportionality coefficient and β depends on the micro-architecture of the material. In our case $\tilde{E}$ is the Young modulus of graphene, which composes the nanotrusses. FCC nanotrusses, where each node is connected to 12 first neighbors with similar struts, present a stretching-dominated response [10]. Indeed, the octet-truss satisfies Maxwell's criterion for static determinacy. This criterion in three dimensions is given by

$$b - 3j + 6 \geq 0 \tag{7}$$

where b and j are the number of struts and nodes, respectively, in the unit cell. For this type of octet-truss lattice material [10] $\alpha = 0.3$ and $\beta = 1$. Contrarily, for bending-dominated structures such as foams, the scaling relation Eq. (6) is satisfied with $\alpha = 1$ and $\beta = 2$ [2]. The scaling relations of our nanotrusses reasonably lie between these two limiting cases.

Due to the number of parameters that influence the scaling relations, one should test different geometries, unit cell dimensions and numbers of layers. This analysis would be interesting, however it would require extensive simulations beyond the scope of our work.

We plan to use the scaling relation Eq. (6) to estimate the average Young modulus $\tilde{E}$ of the graphene sheets that compose the nanotruss networks, using as coefficients and exponents those valid in the limiting cases of linear and parabolic scaling laws. Furthermore, we use the bulk density $\tilde{\rho}$ of graphite ($\tilde{\rho} = 2250$ kg m^{-3}). Due to the presence of defects in the nanotrusses one can expect a reduction of the Young modulus of our structures with respect to graphene ($\tilde{E} = 1.0$ TPa [43]) to values typically found in nanometric graphene sheets (in the range 100 − 500 GPa [6]).

In Table 5 we report the computed Young modulus of graphene in the case of a linear and a parabolic density scaling law. We note that the estimated Young modulus is indeed lower than pristine graphene and is in the range 100 − 500 GPa.

While we use a linear and a parabolic scaling law to estimate the intrinsic Young modulus of graphene, for tannin-derived carbon-based foams the exponent appearing in Eq. (6) was found to be close to 3 [8]. A similar value, was also found for silica aerogels by Gross and Fricke [15]. To reach this value, higher than what can be obtained by simple scaling of the foam, a number of dangling struts were introduced by the authors. Since our nanotruss networks do not present “elastically ineffective” parts, we consider 2.0 a reasonable upper bound for the exponent of Eq. (6). Interestingly, a Young modulus of 16 MPa for a density of 0.055 relative to the bulk can be achieved with tannin-derived carbon-based foams [8]. However, since we do not know the exact scaling density relation for our nanotruss networks, a comparison between the mechanical properties of these two types of structures is not presently conceivable.

4.6. Energy absorption

Due to the possible application of nanotruss networks to impact absorption, it is important to study the mechanical behavior of nanotrusses and compare that behavior with standard materials for energy absorption.

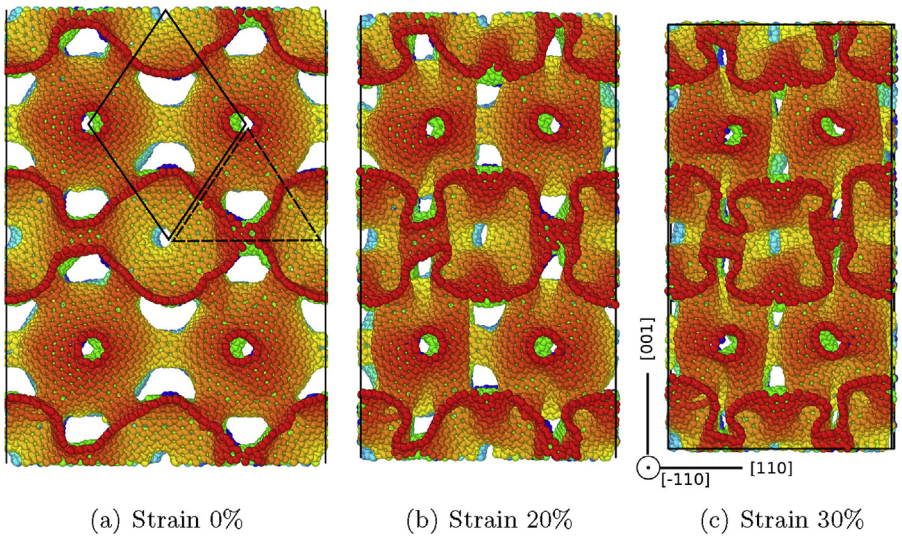

Fig. 11. Three snapshots of sample 3 under uni-axial compression in the [110] direction at 0%, 20% and 30% strain. In image a) are shown the positions of an octahedron and a tetrahedron. In this case the load is aligned with an edge of each tetrahedron. Due to the nanotube insertion there is a contraction in the transverse [001] direction. The Poisson ratio with respect to this direction has negative values for strain higher than 10%. With respect to the [−110] direction (out of the page) the Poisson ratio is initially positive and then tends to zero as strain increases to 30%. The images are to scale. (A colour version of this figure can be viewed online.)

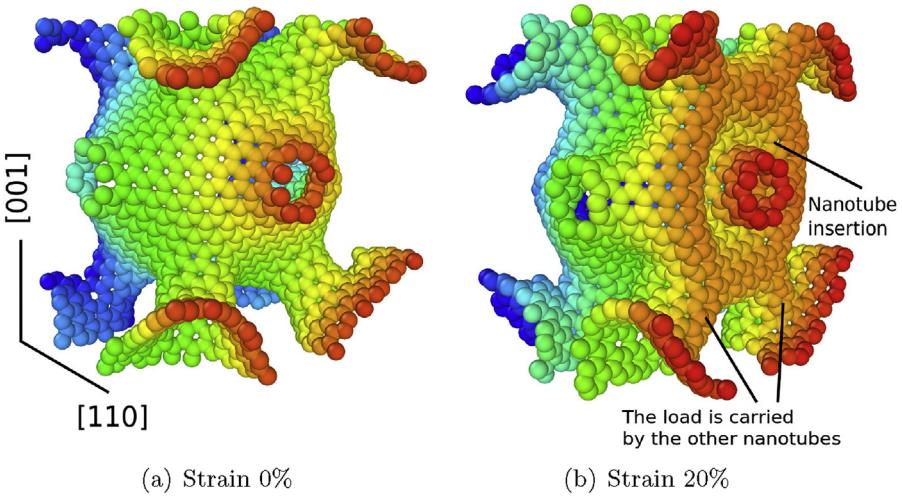

Fig. 12. The two snapshots show a single sphere of sample 3 under uni-axial compression in the [110] direction at 0% and 20% strain. Panel a) shows the undeformed sphere. Panel b) reports the sphere during the deformation. (A colour version of this figure can be viewed online.)

The compressive stress-strain curves can be used to assess the performance of a material with regard to its energy absorption properties. Owing to the similarity of the stress-strain curves of our samples to those typical of absorber materials, we evaluated the most relevant quantities used to describe this property, such as:

the *crush force efficiency*

$$\eta(\varepsilon) = \frac{F_{av}(\varepsilon)}{F_{max}(\varepsilon)} \tag{8}$$

where $F_{av}(\varepsilon)$ is the average of the stress between 0 and ε strain and $F_{max}(\varepsilon)$ is the maximum stress up to strain ε. For the ideal energy absorber, $\eta = 1$.The *stroke efficiency*

$$S_E = \varepsilon_{dens} \tag{9}$$

that represents the strain on the edge of densification and gives an estimation of the ratio between the useful length to absorption and the total length.

The *specific energy absorption* is the energy absorbed per unit of mass

$$SEA = \frac{E_t}{m} \tag{10}$$

where m is the mass, and the *total energy* absorbed

$$E_t(\varepsilon) = V \int_0^{\varepsilon} \sigma\left(\varepsilon'\right) \mathrm{d}\varepsilon' \tag{11}$$

is the area under the stress-strain curve up to strain ε times the sample's volume V.

All previous quantities, except the stroke efficiency, are functions of the strain and in order to compare different materials they are usually evaluated at the densification strain ε_{dens}. The

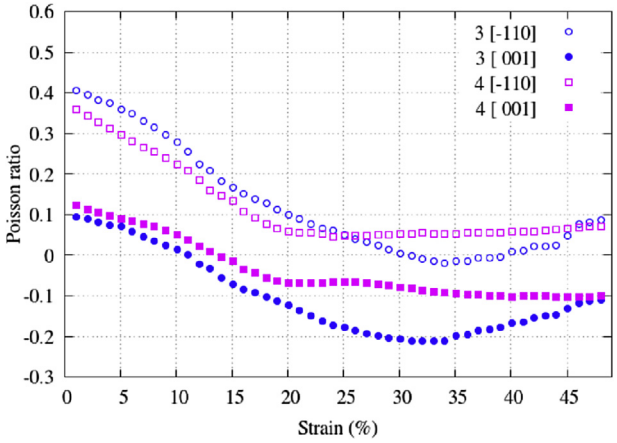

Fig. 13. Poisson ratio of samples 3 and 4 under compression in the [110] direction. The Poisson ratios are between the [110] direction (of load) and the other two directions, [−110] and [001] as indicated by the labels. See Fig. 11 for graphical representation of the axes. These two samples present an auxetic response (negative Poisson ratio) for large deformations. (A colour version of this figure can be viewed online.)

Table 5
Relative density with respect to graphene, Young modulus of graphene that constitutes the nanotruss networks, calculated by means of the relation in Eq. (6) with $\alpha = 0.3$ and $\beta = 1$ (linear relation) or $\alpha = 1$ and $\beta = 2$ (parabolic relation).

Sample	Relative density (%)	Young modulus l inear relation (GPa)	Young modulus parabolic relation (GPa)
1	28.2	319.4	340.1
2	31.4	350.1	334.2
3	31.3	383.0	366.7
4	30.8	455.2	444.0

densification strain is evaluated so as to maximize the *energy absorption efficiency* [3,22]

$$\eta_t(\varepsilon) = \frac{1}{\sigma(\varepsilon)} \int_0^{\varepsilon} \sigma(\varepsilon')\, \mathrm{d}\varepsilon' \tag{12}$$

These quantities are reported in Table 6 for the four samples compressed in the [111] direction. The amount of absorbed energy is reported at 50% strain, a standard strain for the evaluation of the performance of energy absorption materials. This value is higher than $\varepsilon_{\mathrm{dens}}$ for some samples, however for comparative purposes is preferable to choose a common value for strain. The best performances are obtained for sample 4. We compare these values to those of typical absorbers, such as aluminum foams, high strength steel or bulk aluminum. The order of magnitude of the specific energy absorption in aluminum foams, high strength steel and bulk aluminum is of about 10^{-2} MJ kg^{-1}, thus much lower than that of the carbon nanotruss networks we studied in this work.

Table 6
Crush force efficiency, stroke efficiency, and specific energy absorption calculated up to 50% strain for the four samples under uni-axial compression in the [111] direction.

Sample	Crush force efficiency η	Stroke efficiency S_E (%)	Specific energy absorption compression 50% (MJ kg^{-1})	Specific energy loading-unloading 50% (MJ kg^{-1})
1	0.7	47	1.2	0.5
2	0.6	43	1.4	1.0
3	0.5	42	1.2	0.3
4	0.7	40	1.6	0.8

5. Conclusions

The mechanical properties of carbon nanotruss networks in both tensile and compressive regimes were investigated using atomistic simulations with a reactive potential. Our simulations were performed by stretching various nanotruss configurations along the symmetric orientations [100], [110], [111].

First we discussed a method suitable for obtaining realistic structures taking into account the presence of defects. We used the stiffness matrix as a tool to analyze the anisotropy of the samples, finding a small anisotropy due to the nano-structure of our material and the limited box length of the unit cell used during the Voronoi dualization. The presence of pre-strained graphene sheets inside the sample can change the mechanical properties such as the Young modulus, when this is computed for small deformations. We find that this is principally due to the pre-strained nature of our realistic configurations.

Mechanical properties of nanotruss networks are strongly influenced by the presence of defects because these are the points at which cracks nucleate. Nanotruss networks have a brittle nature inherited from the parent material, graphene. Furthermore, we found a parabolic trend of the stress-strain curves under tensile load with the tensile strength roughly proportional to the Young modulus. The Young modulus is comparable to that of bulk metals like aluminum.

Our results show the emergence of different responses in compression as a function of orientation and truss geometry. In particular, we have found that the non linear response related to the partial insertion of the nanotubes inside the spheres is screened in the [111] direction. In this case, a suitable choice of the lattice parameters (as done in sample 3) allows a plateau to be obtained in elastic regime. This elastic response is amenable to the developments of materials that allow the absorption of energy without plastic deformation.

A local unstable insertion of the nanotubes in the spheres was found in the [110] direction for a proper choice of truss geometry. The first type of instability influences the mechanical properties, whereas the main effect of the second instability is to deliver a negative Poisson ratio, as found in particular configurations of nanotrusses (samples 3 and 4). Density scaling relations for nanotruss networks were analyzed assuming a linear or a parabolic relation between relative density and relative Young modulus to estimate the Young modulus of defective graphene that constitutes the nanotruss networks. A range of possible values in accordance with the literature was found.

Finally, energy absorption properties of these carbon nanotrusses have been studied. We found that nanotruss networks could indeed outperform typical materials used as means of energy absorption, such as aluminum foams, high strength steel or bulk aluminum, due to an increased specific energy absorption.

Based on the results of this study, nanotruss networks may represent candidates for porous, flexible, and high strength materials. Finally, the novel properties found in carbon nanotruss networks can greatly advance engineering fields, such as impact energy absorption as well as structural mechanics.

Acknowledgments

N.M.P. is supported by the European Research Council (ERC StG Ideas 2011 BIHSNAM n. 279985, ERC PoC 2015 SILKENE nr. 693670) and by the European Commission under the Graphene Flagship (WP14 “Polymer composites”, no. 696656). S.T and G.G. acknowledge funding from this last grant. The authors acknowledge Dr. R. Gabbrielli and Prof. A. Iorio for useful discussions on Voronoi patterning of Lennard-Jones optimized networks and Dr. M.

Christian for providing constructive comments on the manuscript.

References

[1] J.A.C. Alonso, The storage of hydrogen in nanoporous carbons, J. Mexican Chem. Soc. 56 (2012) 261–269.
[2] M. Ashby, The properties of foams and lattices. Philosophical transactions of the royal society a: mathematical, Phys. Eng. Sci. 364 (2006) 15–30.
[3] M. Avalle, G. Belingardi, R. Montanini, Characterization of polymeric structural foams under compressive impact loading by means of energy-absorption diagram, Int. J. Impact Eng. 25 (2001) 455–472.
[4] P. Avouris, C. Dimitrakopoulos, Graphene: synthesis and applications, Mater. Today 15 (2012) 86–97.
[5] R.H. Baughman, D.S. Galvao, Crystalline networks with unusual predicted mechanical and thermal properties, Nature 365 (1993) 735–737.
[6] M. Becton, X. Zeng, X. Wang, Computational study on the effects of annealing on the mechanical properties of polycrystalline graphene, Carbon 86 (2015) 338–349.
[7] A. Cao, Super-compressible foamlike carbon nanotube films, Science 310 (2005) 1307–1310.
[8] A. Celzard, W. Zhao, A. Pizzi, V. Fierro, Mechanical properties of tannin-based rigid foams undergoing compression, Mater. Sci. Eng. A 527 (2010) 4438–4446.
[9] V.R. Coluci, N.M. Pugno, Molecular dynamics simulations of stretching, twisting and fracture of super carbon nanotubes with different chiralities: towards smart porous and flexible scaffolds, Jnl Comp Theo Nano 7 (2010) 1294–1298.
[10] V. Deshpande, N. Fleck, M. Ashby, Effective properties of the octet-truss lattice material, J. Mech. Phys. Solids 49 (2001) 1747–1769.
[11] F. Ding, Y. Lin, P.O. Krasnov, B.I. Yakobson, Nanotube-derived carbon foam for hydrogen sorption, J. Chem. Phys. 127 (2007) 164703.
[12] N.A. Fleck, V.S. Deshpande, M.F. Ashby, Micro-architectured materials: past, present and future. Proceedings of the royal society of London a: mathematical, Phys. Eng. Sci. 466 (2010) 2495–2516.
[13] I. Frank, D.M. Tanenbaum, A. Van der Zande, P.L. McEuen, Mechanical properties of suspended graphene sheets, J. Vac. Sci. Technol. B 25 (2007) 2558–2561.
[14] G. Garberoglio, N.M. Pugno, S. Taioli, Gas adsorption and separation in realistic and idealized frameworks of organic pillared graphene: a comparative study, J. Phys. Chem. C 119 (2015) 1980–1987.
[15] J. Gross, J. Fricke, Proceedings of the second international conference on nanostructured materials scaling of elastic properties in highly porous nanostructured aerogels, Nanostructured Mater. 6 (1995) 905–908.
[16] D. Haberer, D.V. Vyalikh, S. Taioli, B. Dora, M. Farjam, J. Fink, D. Marchenko, T. Pichler, K. Ziegler, S. Simonucci, M.S. Dresselhaus, M. Knupfer, B. Büchner, A. Grüneis, Tunable band gap in hydrogenated quasi-free-standing graphene, Nano Lett. 10 (2010) 3360–3366, http://dx.doi.org/10.1021/nl101066m. PMID: 20695447.
[17] L.J. Hall, V.R. Coluci, D.S. Galvão, M.E. Kozlov, M. Zhang, S.O. Dantas, R.H. Baughman, Sign change of Poisson's ratio for carbon nanotube sheets, Science 320 (2008) 504–507.
[18] A. Hodge, J. Biener, L. Hsiung, Y. Wang, A. Hamza, J. Satcher, Monolithic nanocrystalline Au fabricated by the compaction of nanoscale foam, J. Mater. Res. 20 (2005) 554–557.
[19] W. Humphrey, A. Dalke, K. Schulten, VMD – visual molecular dynamics, J. Mol. Graph. 14 (1996) 33–38.
[20] G. Jung, Z. Qin, M.J. Buehler, Molecular mechanics of polycrystalline graphene with enhanced fracture toughness, Extreme Mech. Lett. 2 (2015) 52–59.
[21] T. Lenosky, X. Gonze, M. Teter, V. Elser, Energetics of negatively curved graphitic carbon, Nature 355 (1992) 333–335.
[22] Q.M. Li, Compressive strain at the onset of densification of cellular solids, J. Cell. Plastics 42 (2006) 371–392.
[23] S. Park, K. Kittimanapun, J.S. Ahn, Y.K. Kwon, D. Tománek, Designing rigid carbon foams, J. Phys. Condens. Matter 22 (2010) 334220.
[24] S. Plimpton, Fast parallel algorithms for short-range molecular dynamics, J. Comput. Phys. 117 (1995) 1–19.
[25] T.A. Schaedler, A.J. Jacobsen, A. Torrents, A.E. Sorensen, J. Lian, J.R. Greer, L. Valdevit, W.B. Carter, Ultralight metallic microlattices, Science 334 (2011) 962–965.
[26] O.A. Shenderova, D.W. Brenner, A. Omeltchenko, X. Su, L.H. Yang, Atomistic modeling of the fracture of polycrystalline diamond, Phys. Rev. B 61 (2000) 3877–3888.
[27] S.J. Stuart, A.B. Tutein, J.A. Harrison, A reactive potential for hydrocarbons with intermolecular interactions, J. Chem. Phys. 112 (2000) 6472.
[28] A. Stukowski, Visualization and analysis of atomistic simulation data with OVITO–the Open Visualization Tool, Model. Simul. Mater. Sci. Eng. 18 (2010) 015012.
[29] M. Tagami, Y. Liang, H. Naito, Y. Kawazoe, M. Kotani, Negatively curved cubic carbon crystals with octahedral symmetry, Carbon 76 (2014) 266–274.
[30] S. Taioli, R. Gabbrielli, S. Simonucci, N.M. Pugno, A. Iorio, Lobachevsky crystallography made real through carbon pseudospheres, J. Phys. Condens. Matter 28 (2016) 13LT01.
[31] R. Tatti, L. Aversa, R. Verucchi, E. Cavaliere, G. Garberoglio, N.M. Pugno, G. Speranza, S. Taioli, Synthesis of single layer graphene on Cu(111) by C60 supersonic molecular beam epitaxy, RSC Adv. 6 (2016) 37982–37993.
[32] H. Terrones, A.L. Mackay, Triply periodic minimal surfaces decorated with curved graphite, Chem. Phys. Lett. 207 (1993) 45–50.
[33] H. Terrones, M. Terrones, W.K. Hsu, Beyond c60: graphite structures for the future, Chem. Soc. Rev. 24 (1995) 341.
[34] A.P. Thompson, S.J. Plimpton, W. Mattson, General formulation of pressure and stress tensor for arbitrary many-body interaction potentials under periodic boundary conditions, J. Chem. Phys. 131 (2009) 154107.
[35] S.J. Townsend, T.J. Lenosky, D.A. Muller, C.S. Nichols, V. Elser, Negatively curved graphitic sheet model of amorphous carbon, Phys. Rev. Lett. 69 (1992) 921–924.
[36] E. Tylianakis, G.K. Dimitrakakis, S. Melchor, J.A. Dobado, G.E. Froudakis, Porous nanotube network: a novel 3-D nanostructured material with enhanced hydrogen storage capacity, Chem. Commun. 47 (2011) 2303–2305.
[37] L. Valdevit, S.W. Godfrey, T.A. Schaedler, A.J. Jacobsen, W.B. Carter, Compressive strength of hollow microlattices: experimental characterization, modeling, and optimal design, J. Mater. Res. 28 (2013) 2461–2473.
[38] X. Wang, G. Sun, P. Chen, Three-dimensional porous architectures of carbon nanotubes and graphene sheets for energy applications, Front. Energy Res. 2 (2014).
[39] J. Wu, J. He, Z. Zhang, Fracture and negative Poisson's ratio of novel spanned-fullerenes nanotube networks under tension, Comput. Mater. Sci. 80 (2013) 15–26.
[40] X. Xiao, T.E. Beechem, M.T. Brumbach, T.N. Lambert, D.J. Davis, J.R. Michael, C.M. Washburn, J. Wang, S.M. Brozik, D.R. Wheeler, D.B. Burckel, R. Polsky, Lithographically defined three-dimensional graphene structures, ACS Nano 6 (2012) 3573–3579.
[41] J. Yin, X. Li, J. Zhou, W. Guo, Ultralight three-dimensional boron nitride foam with ultralow permittivity and superelasticity, Nano Lett. 13 (2013) 3232–3236.
[42] J.C. Yoon, J.S. Lee, S.I. Kim, K.H. Kim, J.H. Jang, Three-dimensional graphene nano-networks with high quality and mass production capability via precursor-assisted chemical vapor deposition, Sci. Rep. 3 (2013).
[43] H. Zhao, K. Min, N.R. Aluru, Size and chirality dependent elastic properties of graphene nanoribbons under uniaxial tension, Nano Lett. 9 (2009) 3012–3015.

Carbon 116 (2017) 20

Contents lists available at ScienceDirect

Carbon

journal homepage: www.elsevier.com/locate/carbon

Erratum

Erratum to "Designing graphene based nanofoams with nonlinear auxetic and anisotropic mechanical properties under tension or compression" [Carbon 111 (January 2017) 796–806]

Andrea Pedrielli [a, b], Simone Taioli [b, c], Giovanni Garberoglio [b, *], Nicola M. Pugno [a, d, e, **]

[a] Laboratory of Bio-inspired & Graphene Nanomechanics, Department of Civil, Environmental and Mechanical Engineering, University of Trento, Via Mesiano 77, 38123, Trento, Italy
[b] European Center for Theoretical Studies in Nuclear Physics and Related Areas (ECT*-FBK) and Trento Institute for Fundamental Physics and Applications (TIFPA-INFN), 38123, Trento, Italy
[c] Faculty of Mathematics and Physics, Charles University, 180 00, Prague 8, Czechia
[d] Center for Materials and Microsystems, Fondazione Bruno Kessler, Via Sommarive 18, 38123, Povo, TN, Italy
[e] School of Engineering and Materials Science, Materials Research Institute, Queen Mary University of London, London, E1 4NS, UK

The publisher regrets that the Graphical Abstract was not updated and the Supplementary material was not uploaded. The publisher would like to apologise for any inconvenience caused.

Appendix A. Supplementary data

Supplementary data related to this article can be found at http://dx.doi.org/10.1016/j.carbon.2017.01.064.
mmc1.docx: Unit_Cell_A.docx
mmc2.docx: Unit_Cell_B.docx
mmc3.docx: Unit_Cell_C.docx
mmc4.docx: Unit_Cell_D.docx

DOI of original article: http://dx.doi.org/10.1016/j.carbon.2016.10.034.
* Corresponding author.
** Corresponding author. Laboratory of Bio-inspired & Graphene Nanomechanics, Department of Civil, Environmental and Mechanical Engineering, University of Trento, Via Mesiano 77, 38123 Trento, Italy.
E-mail addresses: garberoglio@ectstar.eu (G. Garberoglio), nicola.pugno@unitn.it (N.M. Pugno).

http://dx.doi.org/10.1016/j.carbon.2017.01.064
0008-6223/